Finite Beam Elements for Variable Stiffness Structures

T. Macquart*, A. Pirrera†, and P. M. Weaver‡

Bristol Composite Institute (ACCIS)

University of Bristol, BS8 1TR, United Kingdom

I. Introduction

Current aircraft wings and wind turbine blades are lighter, slender and more flexible than their predecessors. Due to the increasing slenderness and compliance, wings and blades can no longer be assumed to be torsionally rigid, as small torsional deflections can significantly influence their aeroelastic responses. Capturing the flexibility of modern aerospace structures with numerical models is, consequently, crucial to further improving their aeroelastic efficiency [1,2]. However, highly refined, and thus computationally expensive models are generally required to obtain accurate results [3,4], leading to long run-times, which contrasts with the rapid structural performance evaluation needed for optimisation. Considering the increased reliance on numerical simulations and the critical choices that must be made during early design stages, this paper focuses on the development of a rapid, yet accurate, finite element (FE) beam model for the preliminary design of slender structures.

FE analysis employing beam elements is a common design tool for slender structures [5]. The need for beam models able to capture structural couplings resulting from non-conventional, non-uniform cross-sections, and geometric non-linearities has been a significant driver towards the development of refined beam theories [6–9]. In contrast to these refined theories, aimed at capturing high-order deformations, we focus on the improvement of beam elements derived by axiomatic formulations [10]; The issue of spurious nodal strains observed at the interface between elements [11] being central to this work. Although a converged strain state can be reached with mesh refinement, the incurred rise in computational cost conflicts with the need for cheap structural calculations. The goal of this work is to enhance beam elements to reach converged strain

*Lecturer, ACCIS. Corresponding author. E-mail address: terence.macquart@bristol.ac.uk
†Senior Lecturer in Composite Structures and EPSRC Research Fellow, ACCIS, AIAA Member
‡Professor in Lightweight Structures, ACCIS, AIAA Member

fields with fewer nodes than by standard mesh refinement. The two characteristics of conventional beam elements responsible for the appearance of spurious strains, targeted in this work, are: low order polynomial shape functions and the assumption of constant cross-sectional properties (i.e. prismatic elements).

We enhance conventional beam elements by combining the individual merits of polynomial-refinement [12] and variable axial properties [13] into a single numerical framework. First, the generation of N-noded elements (with $N \geq 2$) and their corresponding shape functions (e.g. linear, quadratic, ...) is proposed as a means to smooth strains. Second, element stiffness matrices are calculated employing a spanwise integration method accurately accounting for the variability of structural properties along the element length. Individual effects of the proposed improvements on the accuracy and convergence of beam displacements and strains are investigated using a statically loaded wind turbine blade case study.

II. High Order Beam Elements

Commercial FE packages commonly employ C^0 and C^1 beam elements derived using a displacement-based approach, ensuring displacements C^0, and sometimes first derivative C^1, continuity between elements. However, these elements feature discontinuities in their second and third order derivatives required to evaluate strains, and are as a result not sufficiently accurate in describing strains in non-prismatic beams. In this section, we present a framework to generate high-order beam elements, using an increased number of nodes and higher order polynomial shape functions. In so doing, derived quantities such as strains are more accurately represented than in conventional FE formulations along the element length and at its interfaces.

II.A. Generalised Strains and Displacements

Consider the three dimensional non-prismatic N-noded element illustrated in Figure 1. The notation adopted for the nodal degrees of freedoms (DOFs) includes two subscripts; the first one indicates the node number, the second the axis along which the degree of freedom is active. That is u_{j1}, u_{j2} and u_{j3} denote axial and transverse displacements of node j, while θ_{j1} is the twist angle, and the rotations due to bending deformations are θ_{j2} and θ_{j3}.

Following the axiomatic assumptions associated with Timoshenko's formulation [10], the displacement $\boldsymbol{U}$ of a particle located at a point (x, y, z) along the element is described as

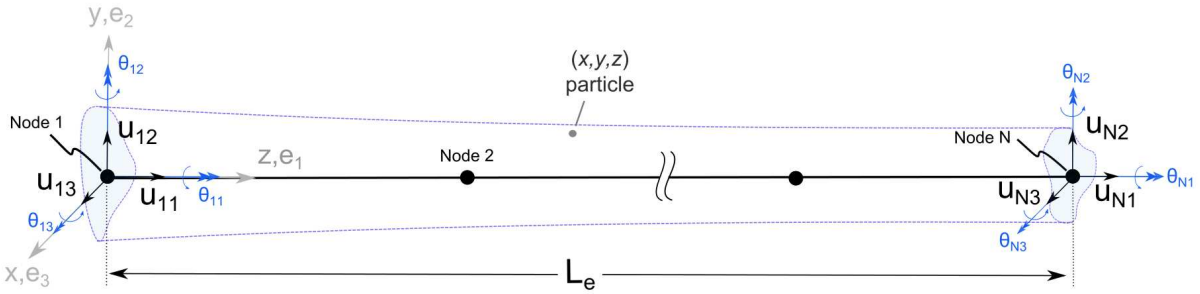

Fig. 1 N-noded beam element

$$\boldsymbol{U} = \begin{bmatrix} U_1(x,y,z) \\ U_2(x,y,z) \\ U_3(x,y,z) \end{bmatrix} = [H]\boldsymbol{U}_{\mathrm{g}} = \begin{bmatrix} 1 & 0 & 0 & 0 & x & -y \\ 0 & 1 & 0 & -x & 0 & 0 \\ 0 & 0 & 1 & y & 0 & 0 \end{bmatrix} \begin{bmatrix} u_1(z) \\ u_2(z) \\ u_3(z) \\ \theta_1(z) \\ \theta_2(z) \\ \theta_3(z) \end{bmatrix}, \tag{1}$$

where $\boldsymbol{U}_{\mathrm{g}}$ is the vector of generalised displacements. The corresponding strains are

$$\begin{cases} \epsilon_{11}(x,y,z) = \frac{\partial \boldsymbol{U}_1}{\partial z} = \frac{\partial u_1}{\partial z} - y\frac{\partial \theta_3}{\partial z} + x\frac{\partial \theta_2}{\partial z} = \epsilon - y\kappa_3 + x\kappa_2 \\ \epsilon_{12}(x,y,z) = \frac{\partial \boldsymbol{U}_1}{\partial y} + \frac{\partial \boldsymbol{U}_2}{\partial z} = -\theta_3 + \frac{\partial u_2}{\partial z} - x\frac{\partial \theta_1}{\partial z} = \gamma_2 - x\kappa_1 \\ \epsilon_{13}(x,y,z) = \frac{\partial \boldsymbol{U}_1}{\partial x} + \frac{\partial \boldsymbol{U}_3}{\partial z} = \theta_2 + \frac{\partial u_3}{\partial z} + y\frac{\partial \theta_1}{\partial z} = \gamma_3 + y\kappa_1 \\ \epsilon_{22} = \epsilon_{33} = \epsilon_{23} = 0 \end{cases}, \tag{2}$$

which can be expressed in vector format as

$$\boldsymbol{\epsilon} = \begin{bmatrix} \epsilon_{11}(x,y,z) \\ \epsilon_{12}(x,y,z) \\ \epsilon_{13}(x,y,z) \\ \epsilon_{22}(x,y,z) \\ \epsilon_{33}(x,y,z) \\ \epsilon_{23}(x,y,z) \end{bmatrix} = [G]\,\boldsymbol{\epsilon}_{\mathrm{g}} = \begin{bmatrix} [H] \\ [0]_{3\times 6} \end{bmatrix} \begin{bmatrix} \epsilon(z) \\ \gamma_2(z) \\ \gamma_3(z) \\ \kappa_1(z) \\ \kappa_2(z) \\ \kappa_3(z) \end{bmatrix}, \tag{3}$$

where $\boldsymbol{\epsilon}_{\mathrm{g}}$ is the generalised strain vector including the beam mid-plane axial strain ϵ, the shear strains γ_2 and γ_3, the torsional rate, κ_1, and two bending strains, κ_2 and κ_3. These are defined as

$$\begin{bmatrix} \epsilon(z) \\ \gamma_2(z) \\ \gamma_3(z) \\ \kappa_1(z) \\ \kappa_2(z) \\ \kappa_3(z) \end{bmatrix} = [\tilde{D}]\boldsymbol{U}_g = \begin{bmatrix} \frac{\partial}{\partial z} & 0 & 0 & 0 & 0 & 0 \\ 0 & \frac{\partial}{\partial z} & 0 & 0 & 0 & -1 \\ 0 & 0 & \frac{\partial}{\partial z} & 0 & 1 & 0 \\ 0 & 0 & 0 & \frac{\partial}{\partial z} & 0 & 0 \\ 0 & 0 & 0 & 0 & \frac{\partial}{\partial z} & 0 \\ 0 & 0 & 0 & 0 & 0 & \frac{\partial}{\partial z} \end{bmatrix} \begin{bmatrix} u_1(z) \\ u_2(z) \\ u_3(z) \\ \theta_1(z) \\ \theta_2(z) \\ \theta_3(z) \end{bmatrix}. \tag{4}$$

Although we chose a C^0 Timoshenko's element as a more general case for this section, C^1 Euler-Bernoulli beam elements are employed in the rest of this paper, without loss of accuracy, to better highlight the effect of the proposed changes on various order of initial shape functions (i.e. linear, quadratic and cubic).

II.B. Shape Functions

In this section, we derive the shape functions associated with N-noded elements. The nodal DOFs of the N-noded element are

$$\boldsymbol{U}_{\mathrm{n}} = [\boldsymbol{U}_{\mathrm{n}1}\ \boldsymbol{U}_{\mathrm{n}2}\ \ldots\ \boldsymbol{U}_{\mathrm{n}N}]^T, \tag{5}$$

where, the DOFs corresponding to node j are

$$\boldsymbol{U}_{\mathrm{n}j} = [u_{j1} \;\; u_{j2} \;\; u_{j3} \;\; \theta_{j1} \;\; \theta_{j2} \;\; \theta_{j3}]^T \, . \tag{6}$$

Following classical FE [14], the generalised displacements $\boldsymbol{U}_{\mathrm{g}}$ are described using polynomial functions. In the case of a C^1 continuous N-noded Euler-Bernoulli beam element, the polynomials are

$$u_1(z) = \sum_{i=0}^{N-1} a_i z^i \quad , \quad \theta_1(z) = \sum_{i=0}^{N-1} d_i z^i. \tag{7}$$

$$u_2(z) = \sum_{i=0}^{2N-1} b_i z^i \quad , \quad \theta_2(z) = \sum_{i=0}^{2N-2} e_i z^i, \tag{8}$$

$$u_3(z) = \sum_{i=0}^{2N-1} c_i z^i \quad , \quad \theta_3(z) = \sum_{i=0}^{2N-2} f_i z^i, \tag{9}$$

where a_i, b_i, ..., f_i are coefficients to be determined. The shape functions are then calculated to express the generalised displacements $\boldsymbol{U}_{\mathrm{g}}$ in terms of the nodal displacement vector, $\boldsymbol{U}_{\mathrm{n}}$, as

$$\boldsymbol{U}_{\mathrm{g}} = [N]\boldsymbol{U}_{\mathrm{n}} = [\boldsymbol{N}_1 \;\; \boldsymbol{N}_2 \;\; \boldsymbol{N}_3 \;\; \boldsymbol{N}_4 \;\; \boldsymbol{N}_5 \;\; \boldsymbol{N}_6]^T \boldsymbol{U}_{\mathrm{n}}, \tag{10}$$

where, $[N]$ is the shape function matrix and $\boldsymbol{N}_1$, ..., $\boldsymbol{N}_6$ are the shape functions corresponding to each generalised displacement. Combining Eqs. (10) and (4) we express the generalised strains as functions of nodal displacements

$$\boldsymbol{\epsilon}_{\mathrm{g}} = [\tilde{D}][N]\boldsymbol{U}_{\mathrm{n}}. \tag{11}$$

The shape functions are obtained by equating the displacements in Eqs. (7)-(9) to their nodal values in Eq. (5). The position of node j, assuming a uniform distribution, along the N-noded element of length L_e is

$$z_j = (j-1)\frac{L_e}{N-1} \quad , \quad \text{for} \quad j = 1, ..., N \quad . \tag{12}$$

Starting with the axial DOF, we equate polynomial (Eq. (7)) and nodal (Eq. (12)) displacements for each

node j to obtain a system of linear equations

$$\left[u_1(z_j) = \sum_{i=0}^{N-1} a_i (z_j)^i = \sum_{i=0}^{N-1} a_i \left((j-1)\frac{L_e}{N-1}\right)^i\right] = u_{j1}, \quad \text{for } j = 1, ..., N \tag{13}$$

that is solved for the coefficients a_i and re-arranged to determine the axial displacement shape functions as shown in Figure 2. For the sake of brevity, only the axial displacement derivation is presented herein.

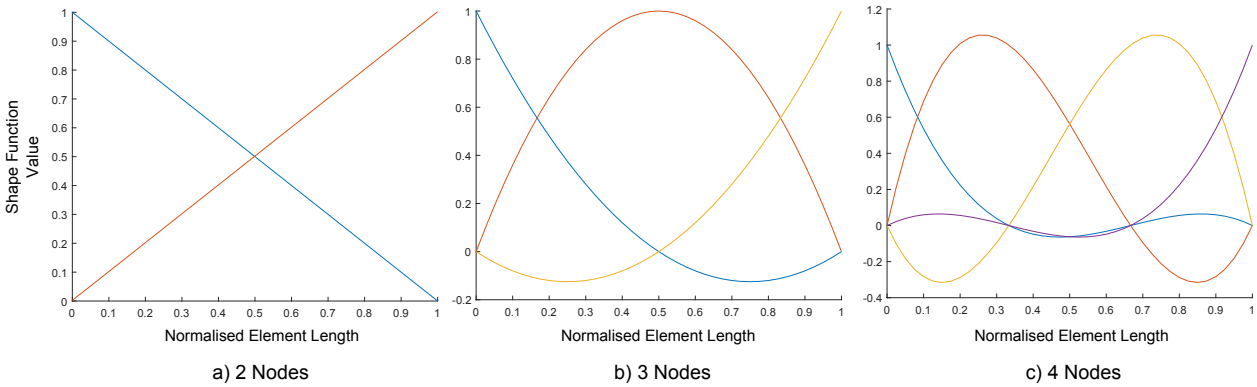

Fig. 2 Axial shape functions for 2-, 3- and 4-noded beam elements

II.C. Stiffness Matrix

The N-noded linear beam element stiffness matrix is derived from the potential strain energy

$$U_{\text{energy}} = \int\int\int \frac{1}{2}\,\boldsymbol{\epsilon}^T\,\boldsymbol{\sigma}\;\, dV, \tag{14}$$

where V represents the element volume. Considering the stress/strain constitutive relation $\boldsymbol{\sigma} = [Q]\boldsymbol{\epsilon}$ where $[Q]$ denotes the material stiffness matrix and substituting the generalised beam strains Eq. (3), and the nodal degrees of freedom Eq. (11) into Eq. (14), we obtain

$$U_{\text{energy}} = \frac{1}{2}\;\boldsymbol{U}_{\text{n}}^T \left[\int\int\int [\,[\tilde{D}N]^T G^T\, QG[\tilde{D}N]]\;\, dV\right] \boldsymbol{U}_{\text{n}}. \tag{15}$$

By identification, the stiffness matrix is

$$[K_e] = \int\int\int [\,[\tilde{D}N]^T G^T\, QG[\tilde{D}N]]\;\, dV. \tag{16}$$

III. Spanwise Stiffness Variability

Prismatic beam elements, assuming constant cross-sectional properties are often used in commercial FE packages. By contrast, we propose a spanwise integration method that captures the variability of structural properties along the element length, mathematically described by re-writing Eq. (16) as

$$[K_e] = \int\int\int [\,[\tilde{D}N]^T G^T\, QG\tilde{D}N]\;\, dV = \int [\tilde{D}N]^T \left[\int\int G^T\, QG dA\right]\;\, [\tilde{D}N]dz = \int [\tilde{D}N]^T [K_{cs}]\;\, [\tilde{D}N]dz, \qquad (17)$$

where $[K_{cs}]$ refers to the symmetric (6×6) cross-sectional stiffness matrix. In contrast to conventional FE where $[K_{cs}]$ is constant over the element length, we employ a varying cross-sectional stiffness matrix such that

$$[K_e] = \int [\tilde{D}N]^T [K_{cs}(z)]\;\, [\tilde{D}N]dz. \qquad (18)$$

Elements are uniformly discretised into M spanwise locations at which cross-sectional properties are evaluated. Polynomial curve fitting is then applied to each of the 21 cross-sectional stiffness parameters over the element length as illustrated in Figure 3. The varying cross-sectional stiffness matrix is then substituted into Eq. (18) and integrated. Note that the proposed integration method makes the implicit assumption that cross-sectional properties vary smoothly along the element. In practice, neither the diagonal nor the non-diagonal cross-sectional stiffness terms have to be smooth or follow linear or quadratic variations. It is clear that for such cases, the structure must be modelled cautiously so as to choose a combination of beam elements and cross-sections capturing the blade varying properties as accurately as possible.

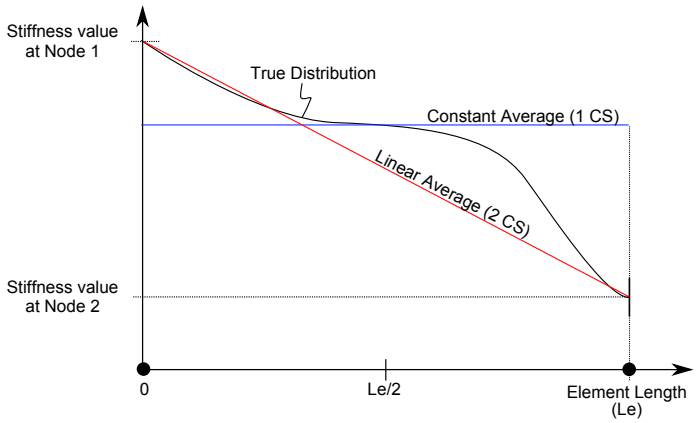

Fig. 3 Constant and linear approximations of structural properties

The accuracy of strain predictions and convergence rates of the beam elements illustrated in Figure 4 are investigated in the rest of this paper. The number of cross-sections dictates the order of polynomial fitting functions used to approximate the variation of structural properties over the element length. The number of beam nodes determines the order of shape functions.

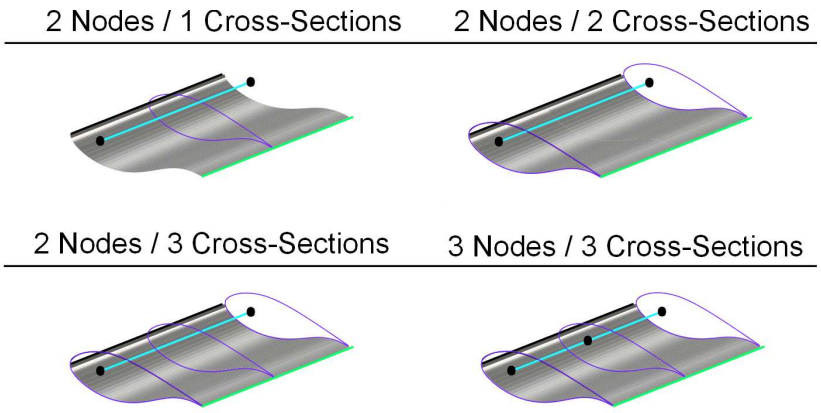

Fig. 4 Beam element configurations investigated

IV. Application

The NREL 5 megawatt wind turbine blade geometry proposed by Jonkman et al. [15] is used as a case study. Note that a bend-twist coupling contribution is added, assuming a linearly increasing coupling coefficient from root to tip, as a means to investigate the effects of our framework on twist predictions.

IV.A. Benchmark Results

We start by generating a benchmark set of displacements and strains obtained with 200 prismatic Euler-Bernoulli beam elements, each with 2 nodes and 1 cross-section. The blade is subjected to a representative force distribution obtained via a static aeroelastic analysis at the turbine rated wind speed [16] . The blade cross-sectional properties, displacements, and strains are presented in Figure 5. In contrast to conventional strain plots based on Gauss points, the strains are plotted at element nodes and the strain distributions along elements are calculated using the shape function derivatives of Eq. (11). This distinction is made to highlight disparities between artificially smoothed and raw strains.

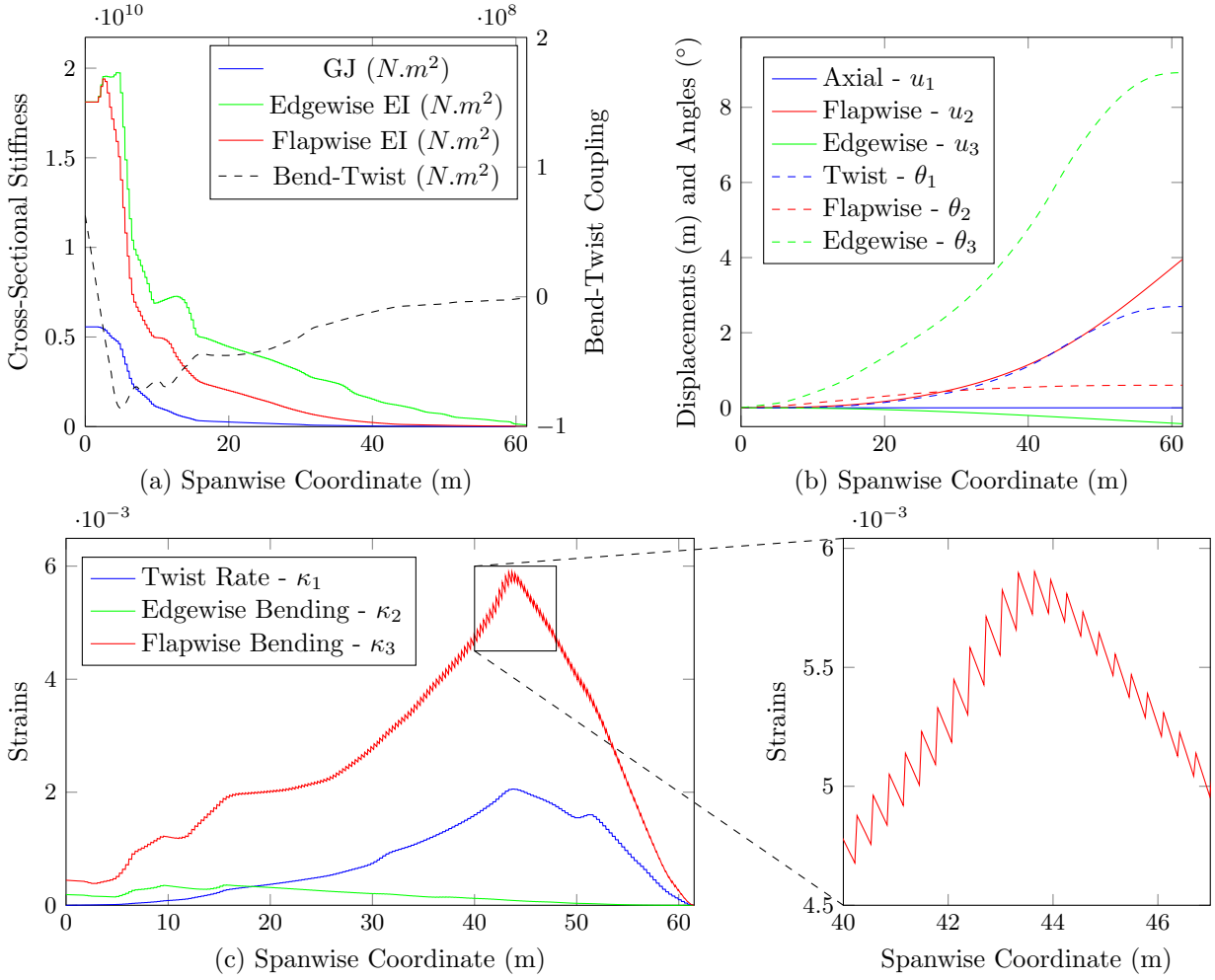

Fig. 5 Blade cross-sectional stiffness (a), displacements (b) and strains (c) - 200 conventional elements

Our goal is to reach a similarly refined state of strains as in Figure 5, but with significantly less DOFs. Since our formulation is displacement-based, a small number of nodes (i.e. 20) is sufficient to obtain converged displacements regardless of the beam elements employed. The strain results obtained with 20 and 200 conventional elements are compared in Figure 6. The significant strain discontinuities observed at interfaces between elements are a direct consequence of the derivative discontinuities at beam nodes as shown in Figure 7.

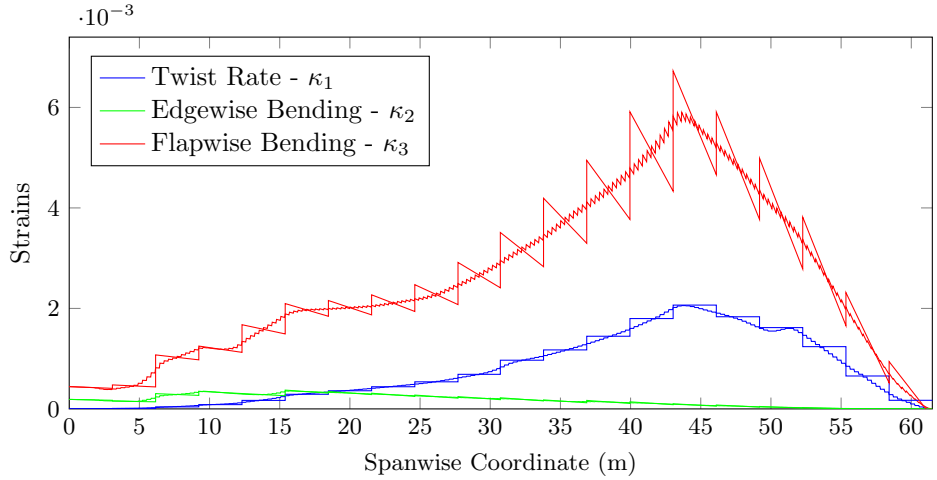

Fig. 6 Bending strains and twist rate - Comparing 200 and 20 conventional elements

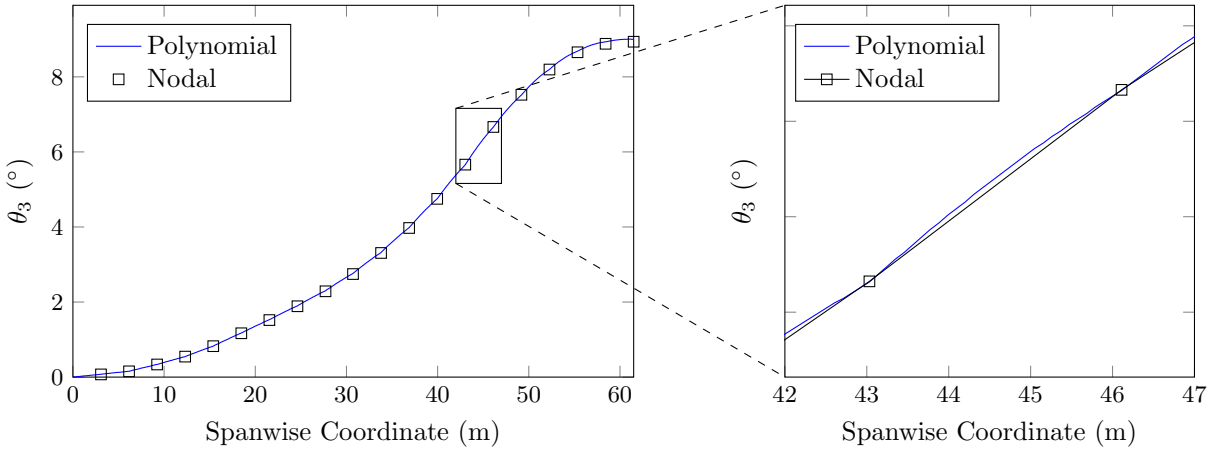

Fig. 7 Zoomed-in bending angle - 20 conventional elements

IV.B. Spanwise Varying Cross-sectional Properties

The effect of spanwise integration on strains is investigated in this section. To this end, we increase the number of cross-sections (CSs). Conventional constant stiffness coefficients (2 Nodes/1 Cross-section) are therefore replaced by linear approximations (2 Nodes/2 Cross-sections) of the spanwise varying properties. Cross-sectional properties and strains are compared in Figure 8. We observe a significant improvement in strain predictions due to the additional cross-sections used to compute the element stiffness matrices. This is an interesting, and somewhat surprising, outcome because strains have been smoothed whilst the order, and therefore complexity, of shape functions has not changed. The better prediction of the elemental stiffness matrix, a cheap computation, is solely responsible for the observed improvement. Bending strains, in particular, are strongly affected because their high order (i.e. cubic) shape function increases the sensitivity to nodal displacement errors. Further examining the results and zooming-in on the displacements, one can

see that a better prediction of the elemental stiffness matrix leads to a reduction in the discontinuities of derivatives at nodal interfaces between elements as evidenced by Figure 9.

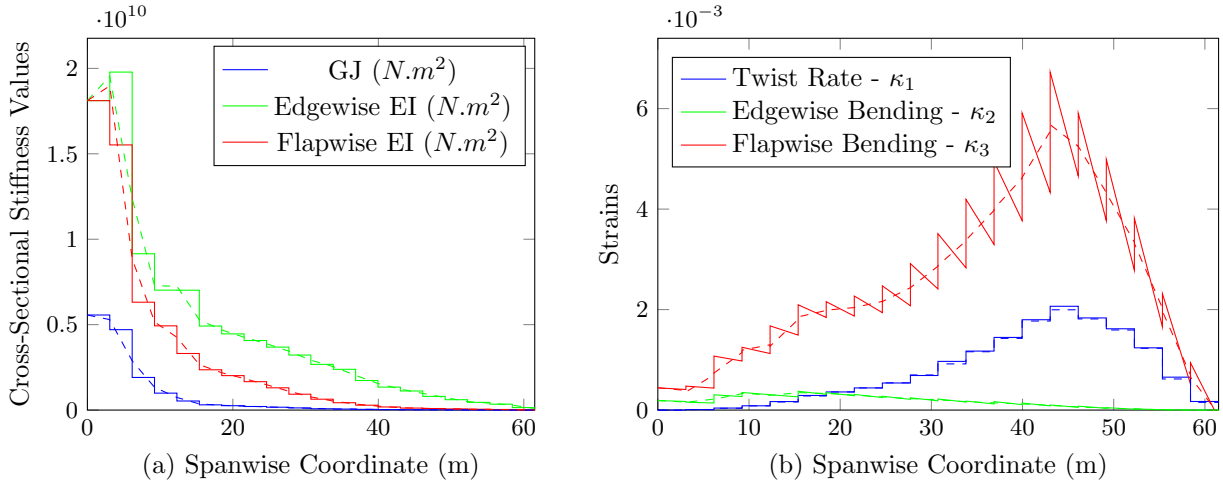

Fig. 8 Piecewise constant (——) and linear (- - -) approximations of cross-sectional properties (a) and strain results (b) - 20 elements

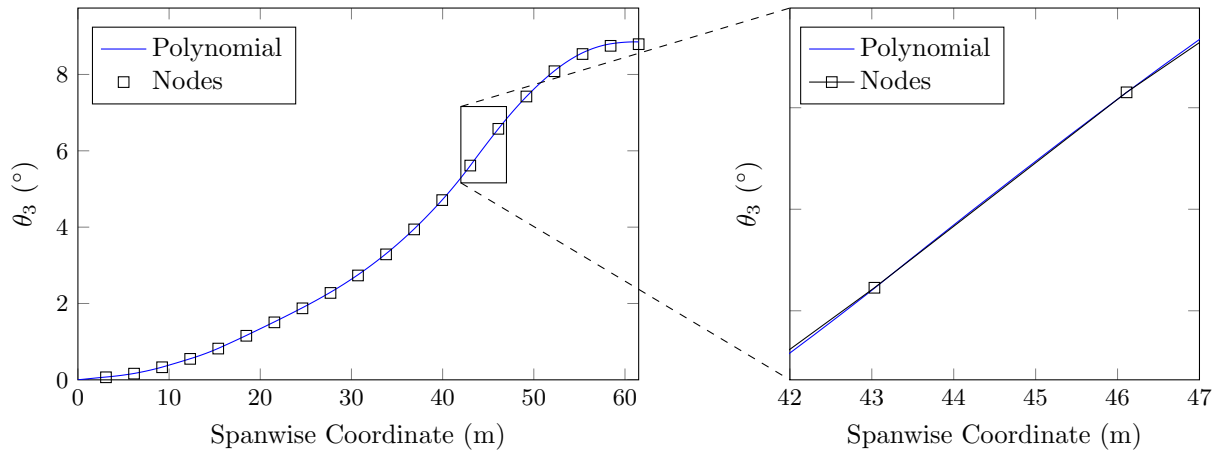

Fig. 9 Zoomed-in bending angles - 20 elements / 2 Cross-sections

IV.C. Variable Number of Nodes and Cross-sections

In this section we simultaneously vary the number of cross-sections and nodes within beam elements. We start with a 3-noded element and 3 cross-sections. Strains are compared against those obtained with 2-noded elements in Figure 10, which shows that by increasing the number of nodes enriches the shape functions and therefore smooth strains. For example, the twist rate becomes linear along each element, while bending strains become quadratic. This comparison highlights the good strain convergence achieved with 3-noded elements and a quadratic variations of spanwise properties (i.e. 3 cross-sections). Elements

with even more nodes could be used. However, using high order polynomials increases computation and affects the conditioning properties of matrices.

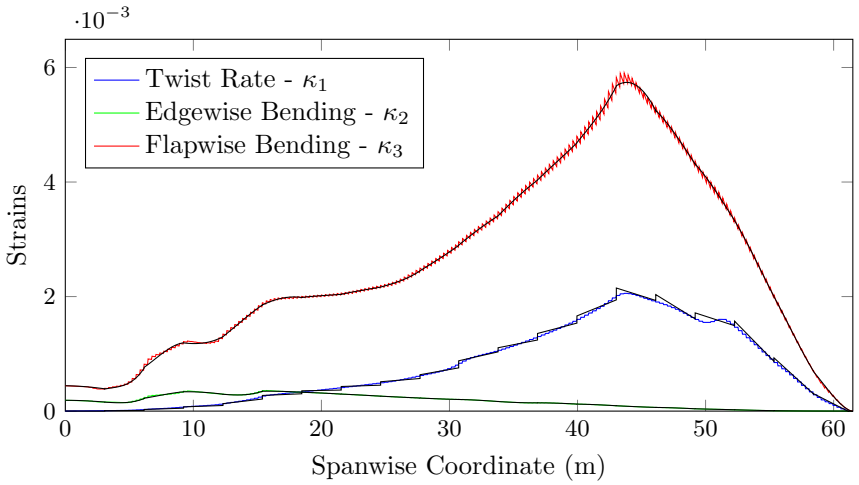

Fig. 10 Strains comparison between 200 conventional elements (——) and 20, 3-noded / 3 cross-sections, elements (——)

Finally, a convergence study is carried out. The computational accuracy and efficiency of the corresponding models is presented in Table 1. Converged static results are normalised based on a highly refined model (i.e. 3846 DOFs) of conventional 2-noded prismatic elements. Three indices, including potential strain energy (Eq. (15)), displacement and strain fields are employed to assess convergence. Additionally, a fourth index evaluates strains smoothness. Normalised displacement and strain field errors, denoted E_{ndf} and E_{nsf}, are calculated as

$$E_{\text{ndf}} = 100 \sum_{i=1}^{\text{N}_{\text{nodes}}} \sum_{j=1}^{\text{N}_{\text{dof}}} \left| \frac{\boldsymbol{U}_{n,ij}^{3846} - \boldsymbol{U}_{n,ij}}{\boldsymbol{U}_{n,ij}^{3846}} \right|, \tag{19}$$

where the nodal displacements $\boldsymbol{U}_n$ are compared and normalised against the interpolated benchmark nodal displacement values $\boldsymbol{U}_n^{3846}$. Similarly, the normalised strain field error is defined as

$$E_{\text{nsf}} = 100 \sum_{i=1}^{\text{N}_{\text{elmt}}} \sum_{j=1}^{\text{N}_{\text{strain}}} \left| \frac{\boldsymbol{\epsilon}_{ij}^{3846} - \boldsymbol{\epsilon}_{ij}}{\boldsymbol{\epsilon}_{ij}^{3846}} \right|, \tag{20}$$

where strains are taken at uniformly distributed locations between nodes. Further to these convergence indices, the continuity index used to evaluate the strain field smoothness is calculated as

$$C_{\text{index}} = \frac{1}{C_{\text{index}}^{3846}} \sum_{i=1}^{\text{N}_{\text{elmt}}} ||\boldsymbol{\epsilon}_{\text{s}} - \boldsymbol{\epsilon}||, \tag{21}$$

in which $\boldsymbol{\epsilon}$ is the strain field distributed over the blade length and $\boldsymbol{\epsilon}_s$ is the smoothed spline fitted to this strain distribution. The resulting index is then normalised with respect to the benchmark smoothness index denoted C^{3846}_{index}.

As observed in Table 1, the model based on conventional prismatic beam elements (i.e. uniform cross-sections) requires 486 DOFs in order for energy, displacement and strain errors to drop below five percent. By comparison, using the same number of nodes, but linearly varying cross-sectional properties, is seen to effectively smooth strains and predict more accurate strains with only 246 DOFs. However, further increasing the number of cross-sections for 2-noded elements does not result in any significant changes. Employing 3-noded / 3 cross-sections elements effectively increases displacements and strains accuracy such that only 126 DOFs are required. In addition, the smoothness of all the proposed element configurations is seen to converge faster than that of conventional 2-noded prismatic elements. In view of the results presented in Table 1, the proposed enhancements provide a means for a two to three fold reduction of the number of DOFs, in comparison to conventional uniform cross-section beam elements.

V. Conclusion

The present paper proposes an enhanced axiomatic beam model for the analysis of slender structures with spatially varying properties. Two typical issues encountered with conventional beam modelling approaches have been addressed. First, a beam element with a variable number of nodes is proposed to smooth nodal strains. Second, a spanwise integration is proposed to improve the quality of the beam stiffness matrices for non-prismatic elements.

Results highlight the basic limitations of conventional beam modelling techniques and support the need for more accurate approaches to model structures with significant level of stiffness variability with fewer DOFs. The application of the proposed elements to a typical wind turbine blade case study was carried out. It is shown that by increasing the order of polynomial functions used to approximate the variation of spanwise properties successfully helps to reduce spurious strains, due to an increased accuracy of the element stiffness matrices. Moreover, increasing the number of nodes in conjunction with the number of cross-sections successfully raises the order of strain distribution functions and therefore leads to smoother strains. Finally, the convergence study has highlighted the computational benefits, i.e. a two to three fold reduction of the number of DOFs.

Table 1 Convergence study of the proposed element configurations

Element Configuration	# DOF	Normalised Energy (%)	Normalised Displacement Field Error (%)	Normalised Strain Field Error (%)	Continuity Index
2-Node Element Uniform Cross-Section	36	123.84	22.73	65.41	161.33
	66	105.53	9.11	29.77	69.40
	126	100.42	4.42	13.71	33.23
	246	100.08	2.52	6.79	16.30
	486	**100.01**	**1.38**	**3.55**	**8.09**
	966	99.98	0.72	1.60	4.02
	1926	100.00	0.30	0.60	2.00
	3846	100.00	0.00	0.00	1.00
2-Node Element Linearly Varying Cross-Section	36	92.87	23.68	10.41	39.49
	66	98.90	12.74	7.98	19.39
	126	99.30	6.48	5.71	8.55
	246	**99.56**	**2.99**	**3.68**	**3.78**
	486	99.88	1.50	2.18	1.74
	966	99.95	0.76	1.27	0.83
	1926	99.99	0.30	0.72	0.40
2-Node Element Quadratically Varying Cross-Section	36	110.87	14.80	20.96	61.96
	66	102.61	7.95	13.05	22.24
	126	100.04	4.46	6.91	8.75
	246	**99.94**	**2.52**	**4.03**	**3.80**
	486	99.97	1.43	2.23	1.74
	966	99.97	0.76	1.28	0.83
	1926	99.97	0.33	0.74	0.40
3-Node Element Quadratically Varying Cross-Section	66	111.22	10.25	11.30	27.17
	126	**102.82**	**3.34**	**4.96**	**6.95**
	246	100.07	2.61	2.59	2.06
	486	99.94	1.45	1.51	0.86
	966	99.97	0.70	1.14	0.47
	1926	99.97	0.29	0.95	0.37

Acknowledgements

The authors would like to acknowledge the support of the EPSRC under its SUPERGEN Wind Challenge 2015 Grant, EP/N006127/1. Supporting data are provided within this paper.

References

[1] Guillaume Francois, Jonathan E Cooper, and Paul Weaver. Aeroelastic tailoring using the spars and stringers planform geometry. In *58th AIAA/ASCE/AHS/ASC Structures, Structural Dynamics, and Materials Conference*, page 1360, 2017.

[2] Timothy R Brooks, Graeme Kennedy, and Joaquim Martins. High-fidelity multipoint aerostructural optimization of a high

aspect ratio tow-steered composite wing. In *58th AIAA/ASCE/AHS/ASC Structures, Structural Dynamics, and Materials Conference*, page 1350, 2017.

[3] Michele Castellani, Jonathan E Cooper, and Yves Lemmens. Nonlinear static aeroelasticity of high-aspect-ratio-wing aircraft by finite element and multibody methods. *Journal of Aircraft*, pages 1–13, 2016.

[4] VA Fedorov, N Dimitrov, Christian Berggreen, Steen Krenk, Kim Branner, and Peter Berring. Investigation of structural behaviour due to bend-twist couplings in wind turbine blades. In *Proceedings of the 17th International Conference of Composite Materials (ICCM), Edinburgh, UK*, 2009.

[5] Noud PM Werter, Jurij Sodja, and Roeland De Breuker. Design and testing of aeroelastically tailored wings under maneuver loading. *AIAA Journal*, pages 1–14, 2016.

[6] Wenbin Yu, Dewey H Hodges, and Jimmy C Ho. Variational asymptotic beam sectional analysis–an updated version. *International Journal of Engineering Science*, 59:40–64, 2012.

[7] R Schardt. Generalized beam theory - an adequate method for coupled stability problems. *Thin-Walled Structures*, 19(2):161–180, 1994.

[8] Erasmo Carrera, Alfonso Pagani, Marco Petrolo, and Enrico Zappino. Recent developments on refined theories for beams with applications. *Mechanical Engineering Reviews*, 2(2):14–00298, 2015.

[9] Liviu Librescu and Ohseop Song. On the static aeroelastic tailoring of composite aircraft swept wings modelled as thin-walled beam structures. *Composites Engineering*, 2(5):497–512, 1992.

[10] Yunhua Luo. An efficient 3d timoshenko beam element with consistent shape functions. *Adv. Theor. Appl. Mech*, 1(3):95–106, 2008.

[11] Julian AT Dow. *A unified approach to the finite element method and error analysis procedures*. Academic Press, 1998.

[12] R Tews and W Rachowicz. Application of an automatic hp adaptive finite element method for thin-walled structures. *Computer Methods in Applied Mechanics and Engineering*, 198(21-26):1967–1984, 2009.

[13] Peng He, Zhansheng Liu, and Chun Li. An improved beam element for beams with variable axial parameters. *Shock and Vibration*, 20(4):601–617, 2013.

[14] Daryl L Logan. *A first course in the finite element method*. Cengage Learning, 2011.

[15] Jason Jonkman, Sandy Butterfield, Walter Musial, and George Scott. Definition of a 5-mw reference wind turbine for offshore system development. *National Renewable Energy Laboratory, Golden, CO, Technical Report No. NREL/TP-500-38060*, 2009.

[16] T Macquart, V Maes, D Langston, A Pirrera, and PM Weaver. A new optimisation framework for investigating wind turbine blade designs. In *World Congress of Structural and Multidisciplinary Optimisation*, pages 2044–2060. Springer, 2017.